Supporting Information

Hierarchically Confined FeNiCoMn Alloy Nanoparticles Enable Durable Bifunctional Air Cathodes for Zinc-Air Batteries

Iram Aziz[a,b], Rabiya Javed Awan[a], Adeel Hashmi[a], Xing Chen[b], Xuhui Hu[b], Wenjing Zhang[b*], Salman Noshear Arshad[a,c,d*]

[a] Department of Chemistry and Chemical Engineering, Syed Babar Ali School of Science and Engineering, Lahore University of Management Sciences, Lahore 54792, Pakistan. E-mail: salman.arshad@lums.edu.pk

[b] Department of Environmental and Resource Engineering, Technical University of Denmark, 2800 Kgs. Lyngby, Denmark. Email: wenz@env.dtu.dk

[c] Department of Materials Science and Engineering, King Fahd University of Petroleum & Minerals, Dhahran, Saudi Arabia

[d] Center for Hydrogen Technologies and Carbon Management, King Fahd University of Petroleum & Minerals, Dhahran, Saudi Arabia.

Experimental Methods

Fabrication of FeNiCoMn Catalyzed CNT@CNFs

An electrospinning precursor was prepared by dissolving polyacrylonitrile (PAN, M_w 150,000 $gmol^{-1}$) and polyvinylpyrrolidone (PVP, M_w = 1,300,000 $gmol^{-1}$) in *N,N*-dimethylformamide (DMF, 99.8%) at a 1:1 mass ratio. The solution was magnetically stirred for 24 h to obtain a homogeneous viscous solution. Electrospinning was carried out under an applied voltage of 20 kV with a needle-to-collector distance of 20 cm. The as-spun nanofibers were collected on aluminium foil and pre-oxidized in air at 250 °C for 2 h. The stabilized nanofibers were then immersed in an ethanol solution containing $FeCl_3$ (0.5 g), $NiCl_2$ (0.25 g), $MnCl_2$ (0.25 g), and $CoCl_2$ (0.25 g) and allowed to soak for 24 h to ensure uniform metal salt impregnation. Subsequently, melamine (3 g, 99%) was added to the mixture and stirred for 5 min, followed by standing at room temperature for 12 h. The solvent was removed using a rotary evaporator, and the resulting solid was dried in a heating oven. Finally, the dried NFs were carbonized under an argon atmosphere at 800 °C for 2 h with a heating rate of 4 °C min^{-1}. During this process, metal/alloy NPs catalyzed the in-situ growth of nitrogen-doped CNTs on the CNF surface. The obtained samples were denoted as FNM-CNT@CNF, FCM-CNT@CNF, FNC-CNT@CNF, NCM-CNT@CNF, and FNCM-CNT@CNF (where F = Fe, N = Ni, C = Co, and M = Mn).

Material Characterization

Powder X-ray diffraction (PXRD) patterns were recorded using a Rigaku XRD-6000 diffractometer with Cu K_α radiation (λ = 0.1542 nm), operating at 40 kV and 30 mA. The surface morphology of the samples was examined using a FEI NOVA NanoSEM 450 scanning electron microscope (SEM), while detailed microstructural analysis was performed using a Titan Analytical 80-300 ST transmission electron microscope (TEM). Elemental composition and distribution were analyzed by energy-dispersive X-ray spectroscopy (EDX) attached to the SEM. X-ray photoelectron spectroscopy (XPS) measurements were carried out using a Thermo Scientific™ Nexsa™ X-ray photoelectron spectrometer to investigate the surface chemical states and elemental composition of the samples.

Electrochemical Characterization

Electrochemical measurements were performed using a BioLogic SP-300 potentiostat. ORR activity was evaluated in a standard three-electrode configuration using a rotating ring disk electrode (RRDE) system. A glassy carbon disk electrode (GCE, disk area = 0.196 cm^2) coated with the catalyst served as the working electrode (WE), while a graphite rod and Ag/AgCl electrode were used as the counter (CE) and reference electrodes (RE), respectively. The electrolyte was 0.1M KOH solution. Catalyst ink was prepared by dispersing 5 mg of finely ground catalyst powder in 1 mL of DMF via ultrasonication for 30 min. Subsequently, 10 µL of 5 wt% Nafion solution was added as a binder. A 5 µL aliquot of the ink was drop cast onto the GCE and allowed to dry naturally, resulting in a catalyst loading of 0.20 mg cm^{-2}. Prior to measurements, the electrolyte (0.1 M KOH) was saturated with either O_2 or Ar for 30

min. For electrode activation, cyclic voltammetry (CV) was conducted for 50 cycles at a scan rate of 50 mV s^{-1} under Ar atmosphere. ORR CV curves were then recorded in O_2-saturated electrolyte at 10 mV s^{-1}. Linear sweep voltammetry (LSV) measurements were performed using a rotating disk electrode (RDE) at rotation speeds ranging from 400 to 2400 rpm. Chronoamperometric stability tests were conducted at 0.70 V vs. RHE and 1600 rpm under continuous O_2 purging for FNCM-CNT@CNF and commercial 20 wt% Pt/C catalysts. The electron transfer number (n) was calculated using the Koutecky-Levich (K–L) equation[1]:

$$\frac{1}{j} = \frac{1}{B\omega^{0.5}} + \frac{1}{j_k}$$

where j is the measured current density, j_K is the kinetic current density, and ω is the angular rotation speed WE. The constant B is given by

$$B = 0.2\, nF(D_{O_2})^{2/3} v^{-1/6} C_{O_2}$$

where F is the Faraday constant (96,485 $Cmol^{-1}$), C_{O_2} is the bulk O_2 concentration (1.2×10^{-6} mol cm^{-1}), D_{O_2} is the O_2 diffusion coefficient in 0.1 M KOH (1.9×10^{-5} cm^2 s^{-1}), ν is the kinematic viscosity of the electrolyte (0.01 cm^2 s^{-1}), and n is the electron transfer number.

OER performance was evaluated in 1 M KOH using a three-electrode configuration, with a GCE (area = 0.196 cm^2) as the WE, Hg/HgO as the RE, and a Pt wire as the CE. LSV measurements were conducted at a scan rate of 10 mV s^{-1}. The electrochemically active surface area (ECSA) was estimated by measuring the double layer capacitance (C_{dl}). CV measurements were recorded in a non-faradaic potential region at scan rates ranging from 2 to 10 mV s^{-1}. The C_{dl} value was calculated from the slope of the plot of the capacitive current density difference (j_a - j_c) versus scan rate at 1.12 V vs. RHE, assuming a specific capacitance (C_s) of 0.04 mF cm^{-2}.

Electrochemical measurements were conducted using reference electrodes and electrolyte concentrations selected in accordance with established best practices for alkaline ORR and OER evaluation. An aqueous 0.1 M KOH solution was used as the supporting electrolyte, in line with common RDE/RRDE ORR benchmarking practice as at this concentration[2], , KOH provides low solution resistance and adequate ionic conductivity while maintaining relatively low viscosity and good mass transport. Furthermore, lower hydroxide concentrations mitigate CO_2-induced bicarbonate formation, which can otherwise alter electrolyte composition and compromise the stability and comparability of ORR measurements with literature data[3-4]. In contrast, OER measurements were performed using a Hg/HgO reference electrode in 1 M KOH. The Hg/HgO electrode is specifically designed for strongly alkaline media and exhibits superior potential stability and compatibility at high pH, where Ag/AgCl electrodes may suffer from chloride leakage or junction instability[5-6]. The use of 1 M KOH for OER testing is a well-established convention in alkaline electrocatalysis, as increasing

hydroxide concentration improves electrolyte conductivity and reduces solution resistance, which is critical at the high anodic current densities relevant to oxygen evolution and practical alkaline electrolysis[7]. Together, these choices ensure accurate potential control, minimized iR drop, and reliable comparison with prior reports in the alkaline electrocatalysis literature.

Zinc-Air Battery Performance

A homemade ZAB was assembled using polished zinc foil as the anode and FNCM-CNT@CNF or a physical mixture of 20 wt% Pt/C and RuO_2 (1:1 mass ratio) supported on carbon paper as the air cathode. A 6 M KOH aqueous solution served as the electrolyte. Galvanostatic charge-discharge (GCD) cycling was carried out at a current density of 10 mA cm^{-2} under ambient conditions using a BioLogic SP-300 battery testing system. Each charge-discharge cycle was operated for 20 min using a recurrent galvanostatic pulse method to evaluate cycling stability and durability.

Results and Discussion

OER study

As mentioned in the main draft, the OER kinetics were further analyzed using Tafel plots derived from the LSV data (Figure 2e). FNCM-CNT@CNF exhibits a Tafel slope of 57.2 mV dec^{-1}, which is markedly smaller than those of FNM-CNT@CNF (72.4 mV dec^{-1}), FNC-CNT@CNF (62.1 mV dec^{-1}), FMC-CNT@CNF (65.6 mV dec^{-1}), MNC-CNT@CNF (108.2 mV dec^{-1}), and RuO_2 (116.9 mV dec^{-1}). The reduced Tafel slope reflects faster reaction kinetics and more efficient charge transfer during the OER process, confirming the kinetic advantage of FNCM-CNT@CNF. The superior OER activity of FNCM-CNT@CNF is attributed to the synergistic interaction between the multi-metal alloy nanoparticles and the three-dimensional CNT@CNF architecture. The presence of multiple transition metals with different atomic sizes and electronegativities induces severe lattice distortion within the alloy nanoparticles, leading to nonequilibrium thermodynamic states[8]. These distorted lattice structures can lower the energy barriers for the adsorption, activation, and transformation of oxygen-containing intermediates (e.g., OH*, O*, and OOH*), thereby accelerating OER kinetics. In addition, the hierarchical CNT@CNF framework enhances electrical conductivity and facilitates rapid oxygen bubble release and electrolyte diffusion, minimizing mass-transport limitations. . Furthermore, the electrochemical double-layer capacitance (C_{dl}), estimated from CV measurements at varying scan rates (Figure 2f), reaches 27.8 mF cm^{-2} for FNCM-CNT@CNF, significantly higher than those of the trimetallic counterparts. The increased C_{dl} suggests a larger electrochemically active surface area, arising from the 3D hierarchical CNT@CNF structure and the high dispersion of multi-metal alloy nanoparticles. It should be noted that C_{dl} is also influenced by morphological factors such as surface roughness and nanotube density and therefore does not solely reflect intrinsic catalytic activity. The promising bifunctional performance of FNCM-CNT@CNF is largely due to the synergistic effects of multi-metal alloying NPs and the hierarchical N-doped carbon architecture. Moreover te combination of the unique physiochemical properties (electronegativity, redox potential, melting point, etc.) of the

four metals i.e., Fe, Ni, Mn, and Co into a multi-metal system boosts the overall performance. EIS measurements were conducted to further elucidate the charge transfer characteristics of the catalysts (Figure S8). FNCM-CNT@CNF exhibits the smallest charge transfer resistance among all investigated catalysts, indicating more efficient electron transport across the electrode-electrolyte interface, consistent with its superior OER performance. The disparities observed in the EIS Nyquist plots are attributed to differences in alloy composition and structural features. The FNCM-CNT@CNF benefits from enhanced configurational entropy, leading to improved alloy homogeneity and optimized electronic structure, which facilitate charge transfer. In contrast, trimetallic counterparts exhibit less uniform metal distribution and inferior conductivity.

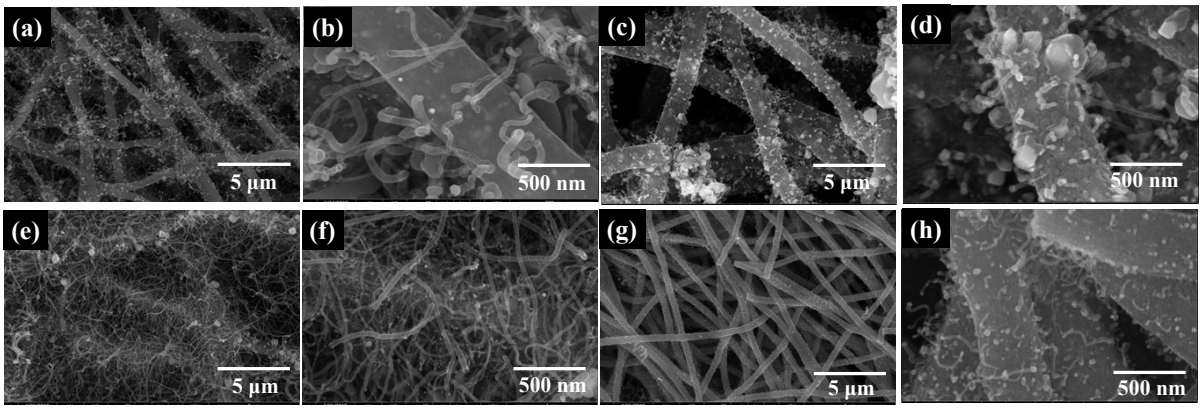

Figure S1 SEM analysis of (a) & (b) MNC-CNT@CNF, (c) & (d) FMC-CNT@CNF, (e) & (f) FNM-CNT@CNF, and (g) & (h) FNC-CNT@CNF at different resolution.

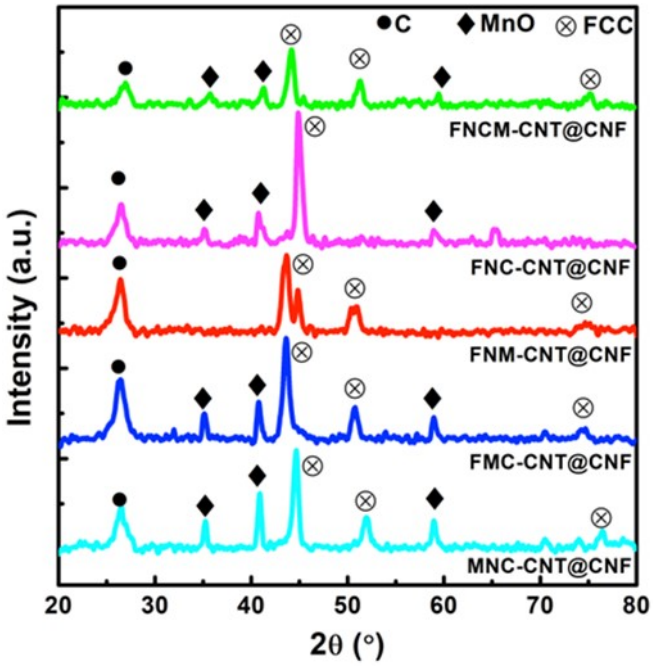

Figure S2: XRD scans of ternary and quaternary NPs containing CNT@CNFs.

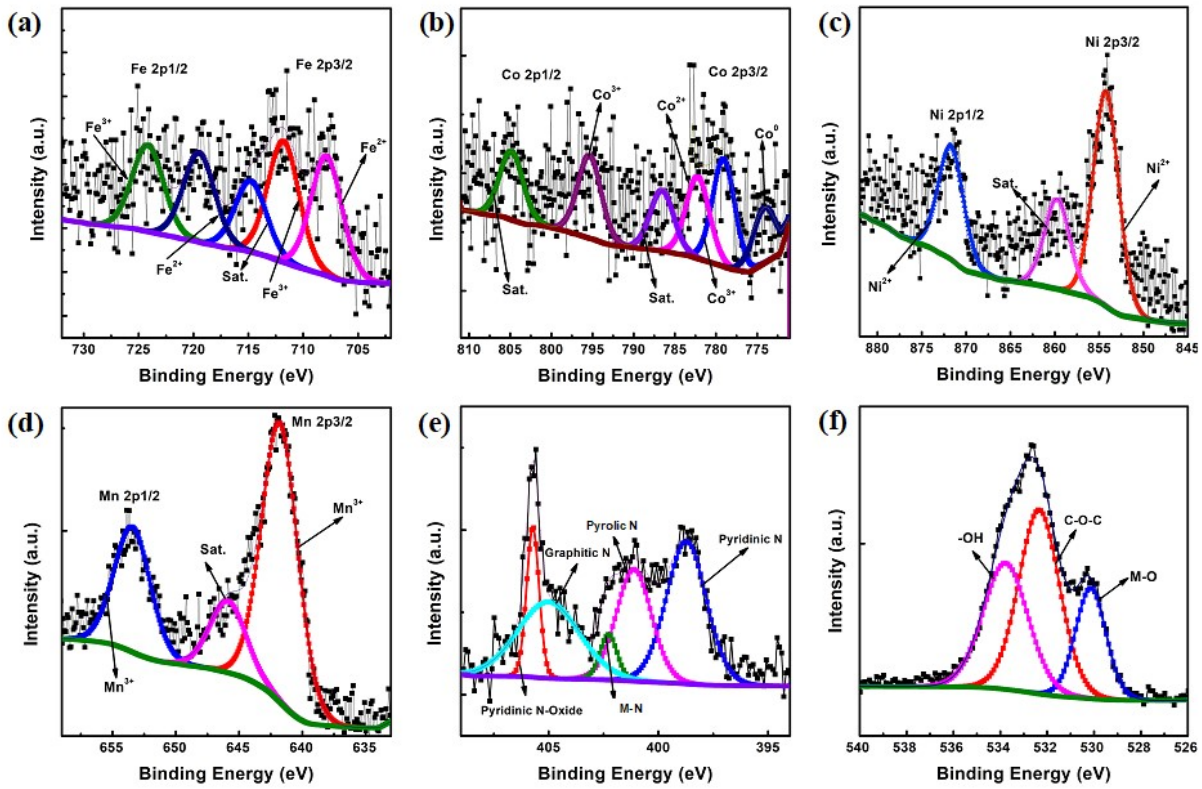

Figure S3 *XPS spectra of (a) Fe 2p, (b) Co 2p, (c) Ni 2p, (d) Mn 2p, (e) N 1s, and (f) O 1s of FNCM-CNT@CNF.*

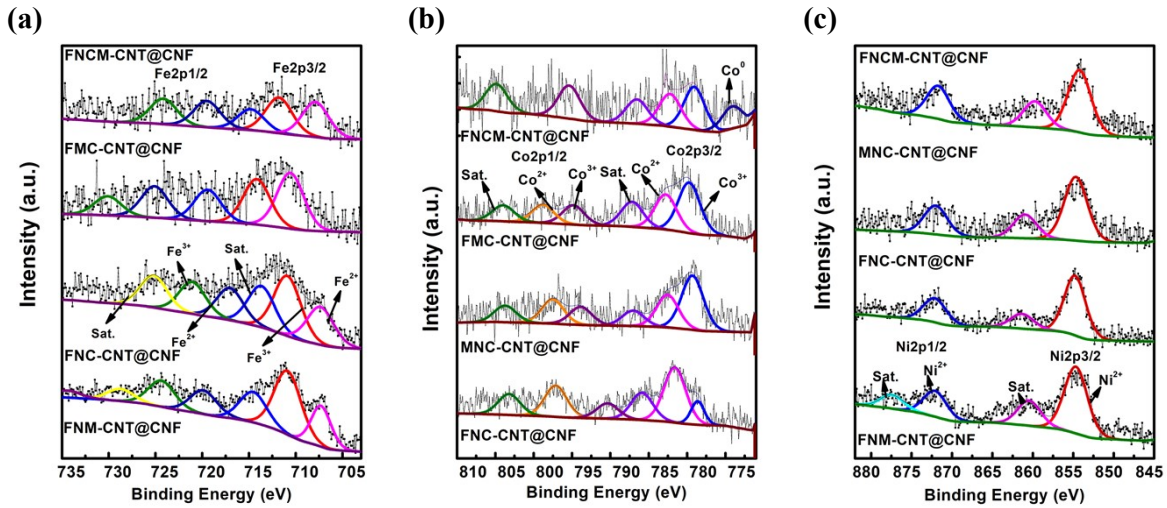

Figure S4 XPS comparison for (a) Fe2p, (b) Co2p, and (c) Ni2p for all prepared electrocatalysts.

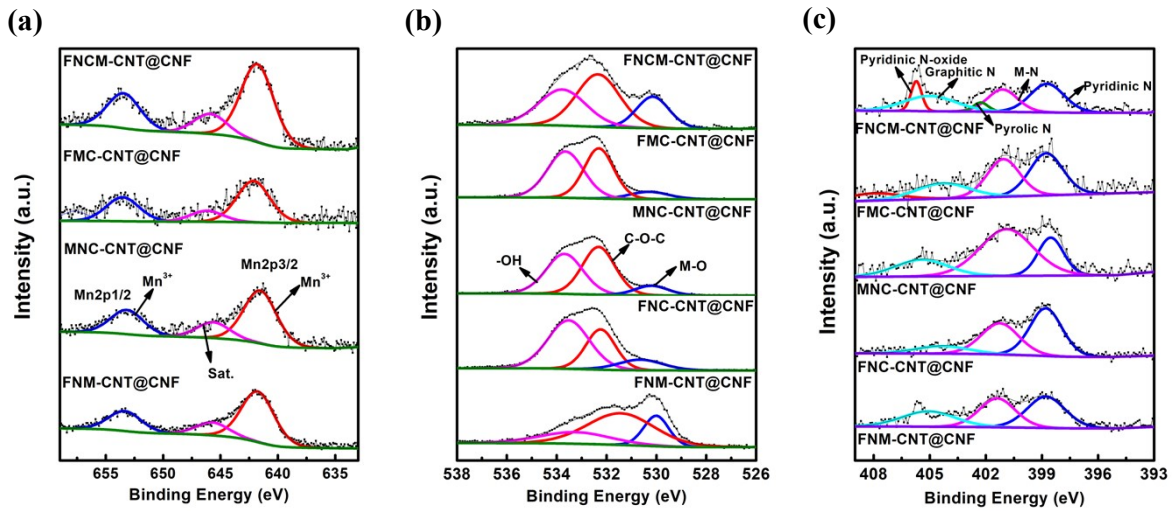

Figure S5 XPS comparison for (a) Mn2p, (b) O1s, and (c) N1s for all prepared electrocatalysts.

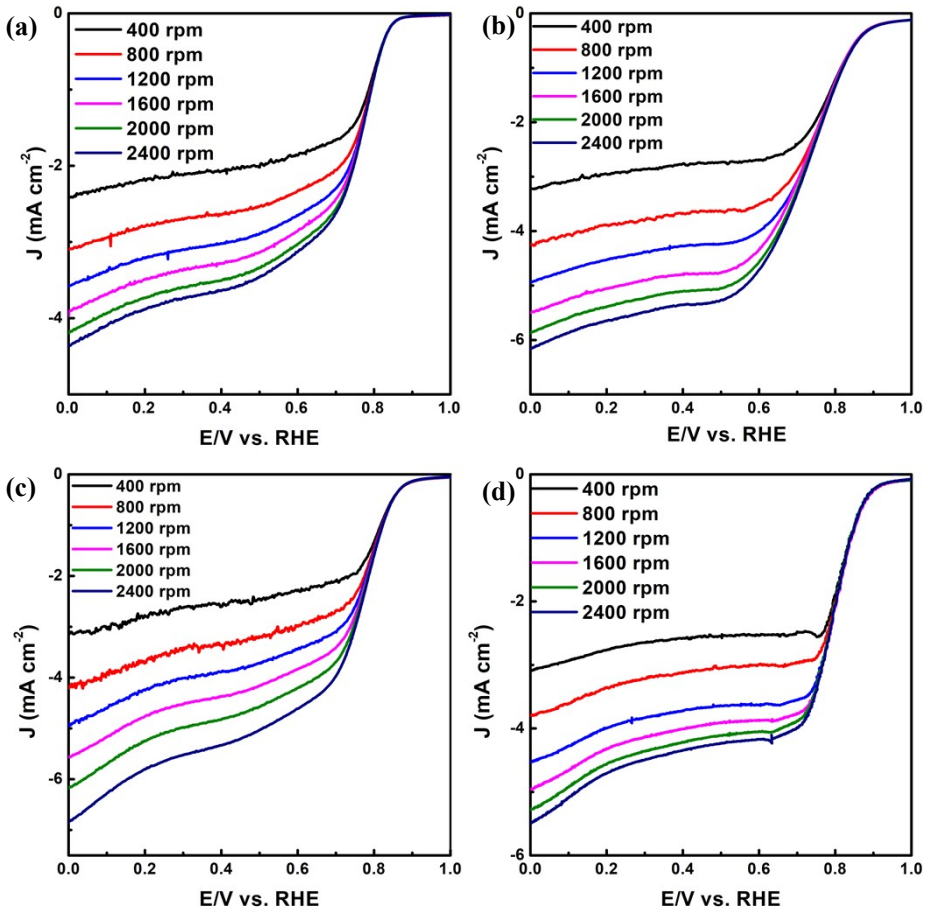

Figure S6 LSV curves of (a) MNC-CNT@CNF, (b) FNM-CNT@CNF, (c) FNC-CNT@CNF, and (d) FMC-CNT@CNF at various rotation speeds.

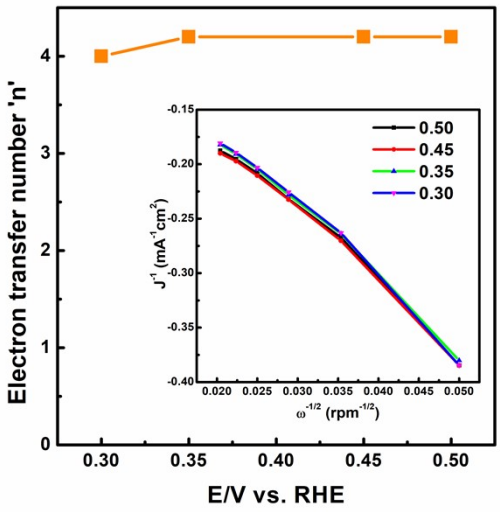

Figure S7: Electron transfer number at variable potentials for FNCM-CNT@CNF, with the inset showing the Koutecky-Levich (K-L) plots.

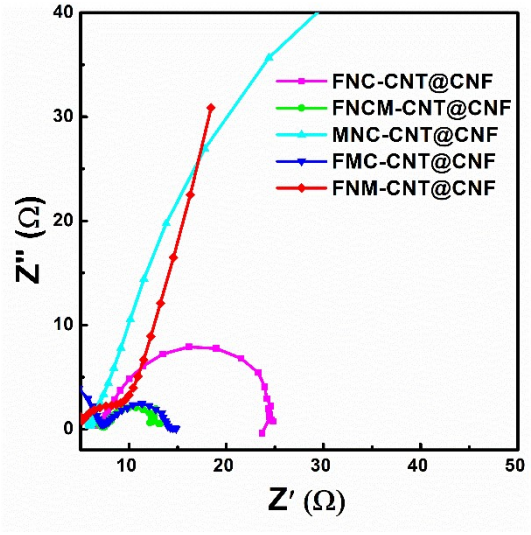

Figure S8: *EIS spectra of FNCM-CNT@CNF compared to other samples.*

Tables S1. Half wave potential for ORR and onset potential (10 $mAcm^{-2}$) for OER with corresponding ΔE values.

Samples	$E_{1/2}(ORR), V$	$E_{j=10}(OER), V$	$\Delta E = E_{j=10} - E_{1/2}, V$
FNCM-CNT@CNF	0.80	1.52	0.72
FNM-CNT@CNF	0.77	1.54	0.77
FNC-CNT@CNF	0.78	1.56	0.78
FMC-CNT@CNF	0.76	1.60	0.84
MNC-CNT@CNF	0.74	1.72	0.98

Table S2. Comparison of FNCM-CNT@CNF for OER/ORR with the recent reported catalysts in literature

Catalyst system	Structure / Support	ORR $E_{1/2}$ (Vvs RHE)	OER η_{10} (mV)	Electrolyte	Ref.
FNCM-CNT@CNF (this work)	FeNiCoMn alloy, graphene-encapsulated, N-CNT@CNF	0.80	290	Alkaline	This work
CrMnFeCoNi HEA	HEA nanoparticles	~0.78	~265	Alkaline	[9]
ZnFeNiCoCr HEA	HEA nanoparticles	~0.86	~305	Alkaline	[10]
FeCo@CoN_x@FeP_x/C	CNT/CNF-derived hybrid	~0.86	~368	Alkaline	[11]
FeNO-CNT-CNFFs	CNT/CNF	~0.87	~430	Alkaline	[12]
MnFeCoNiCu	Carbon support	~0.85	~318	Alkaline	[13]
FeCoNiCrCu	CNF	~0.79	~240	Alkaline	[14]
Cu–Co–Mn–Ni–Fe	Nanoparticles	~0.78	~380	Alkaline	[15]
$La_{0.85}Y_{0.15}Ni_{0.7}Fe_{0.3}O_3$	Nanoparticles	~0.63	~510	Alkaline	[3]

References:

1. Zhou, R.; Zheng, Y.; Jaroniec, M.; Qiao, S.-Z., Determination of the Electron Transfer Number for the Oxygen Reduction Reaction: From Theory to Experiment. *Acs Catalysis* **2016**, *6*, 4720-4728.
2. Bouleau, L.; Pérez-Rodríguez, S.; Quilez-Bermejo, J.; Izquierdo, M.; Xu, F.; Fierro, V.; Celzard, A., Best Practices for Orr Performance Evaluation of Metal-Free Porous Carbon Electrocatalysts. *Carbon* **2022**, *189*, 349-361.
3. Lu, Z.; Zhou, H.; Qian, B.; Wang, S.; Zheng, Y.; Ge, L.; Chen, H., Y and Fe Co-Doped Lanio3 Perovskite as a Novel Bifunctional Electrocatalyst for Rechargeable Zinc-Air Batteries. *International Journal of Hydrogen Energy* **2023**, *48*, 8082-8092.
4. Gebremariam, G. K.; Siraj, K.; Pašti, I. A., Tailoring Electrocatalytic Pathways: A Comparative Review of the Electrolyte's Effects on Five Key Energy Conversion Reactions. *Catalysts* **2025**, *15*, 835.
5. Anantharaj, S.; Sagayaraj, P. J.; Yesupatham, M. S.; Arulraj, R.; Eswaran, K.; Sekar, K.; Noda, S., The Reference Electrode Dilemma in Energy Conversion Electrocatalysis:"Right Vs. Okay Vs. Wrong". *Journal of Materials Chemistry A* **2023**, *11*, 17699-17709.
6. Wei, C.; Rao, R. R.; Peng, J.; Huang, B.; Stephens, I. E.; Risch, M.; Xu, Z. J.; Shao-Horn, Y., Recommended Practices and Benchmark Activity for Hydrogen and

Oxygen Electrocatalysis in Water Splitting and Fuel Cells. *Advanced Materials* **2019**, *31*, 1806296.
7. Liu, J.; Kang, Z.; Li, D.; Pak, M.; Alia, S. M.; Fujimoto, C.; Bender, G.; Kim, Y. S.; Weber, A. Z., Elucidating the Role of Hydroxide Electrolyte on Anion-Exchange-Membrane Water Electrolyzer Performance. *Journal of the electrochemical society* **2021**, *168*, 054522.
8. Xin, Y.; Li, S.; Qian, Y.; Zhu, W.; Yuan, H.; Jiang, P.; Guo, R.; Wang, L., High-Entropy Alloys as a Platform for Catalysis: Progress, Challenges, and Opportunities. *Acs Catalysis* **2020**, *10*, 11280-11306.
9. He, R.; Yang, L.; Zhang, Y.; Wang, X.; Lee, S.; Zhang, T.; Li, L.; Liang, Z.; Chen, J.; Li, J., A Crmnfeconi High Entropy Alloy Boosting Oxygen Evolution/Reduction Reactions and Zinc-Air Battery Performance. *Energy Storage Materials* **2023**, *58*, 287-298.
10. Li, J.; Li, B.; Li, P.-T.; Zhang, N.; Shang, H.-S., A Znfenicocr High-Entropy Alloy for Efficient Bifunctional Oxygen Electrocatalysis. *Rare Metals* **2025**, *44*, 1789-1799.
11. Ding, W.; Saad, A.; Wu, Y.; Wang, Z.; Li, X., Cnts/Cnf-Supported Multi-Active Components as Highly Efficient Bifunctional Oxygen Electrocatalysts and Their Applications in Zinc-Air Batteries. *Nano Research* **2023**, *16*, 4793-4802.
12. Ji, D.; Peng, S.; Safanama, D.; Yu, H.; Li, L.; Yang, G.; Qin, X.; Srinivasan, M.; Adams, S.; Ramakrishna, S., Design of 3-Dimensional Hierarchical Architectures of Carbon and Highly Active Transition Metals (Fe, Co, Ni) as Bifunctional Oxygen Catalysts for Hybrid Lithium–Air Batteries. *Chemistry of Materials* **2017**, *29*, 1665-1675.
13. Chen, Q.; Shi, L.; Xu, G.; Hu, M.; Peng, M.; Yao, Z., Noble Metal-Free Xfeconicu (X= Cr, Mg, and Mn) High Entropy Alloys for Efficient Orr/Oer Bifunctional Catalysis. *Colloids and Surfaces A: Physicochemical and Engineering Aspects* **2025**, *709*, 136106.
14. Xia, L.; Dai, P.; Qu, C.; Yang, Z.; Zhen, H.; Wang, K.; Wu, M., High-Entropy Alloy Self-Supporting Bifunctional Electrocatalysts with Exceptional Performance for Flexible Zinc–Air Batteries. *Journal of Materials Chemistry A* **2025**, *13*, 39382-39392.
15. Madan, C.; Jha, S. R.; Katiyar, N. K.; Singh, A.; Mitra, R.; Tiwary, C. S.; Biswas, K.; Halder, A., Understanding the Evolution of Catalytically Active Multi-Metal Sites in a Bifunctional High-Entropy Alloy Electrocatalyst for Zinc–Air Battery Application. *Energy Advances* **2023**, *2*, 2055-2068.